## Original Article

# A Numerical Investigation of the Effect of Stenosed Trapezoidal Shape Models on Sinusoidal Pulsatile Hemodynamics for Arterial Blood Flow

Md. Jashim Uddin

Department of Applied Mathematics, Noakhali Science and Technology University, Noakhali, Bangladesh.

Corresponding Author: jashim@nstu.edu.bd

Received: 07 August 2025 Revised: 08 September 2025 Accepted: 09 October 2025 Published: 31 October 2025

Abstract - Numerical computations of the flow pulsation in a stenotic vessel are employed to examine the various trapezoidal stenosis shapes' impact on the flow characteristics around the stenotic and post-stenotic zones. The finite element method-based COMSOL Multiphysics software is adopted with a satisfactory verification of the numerical technique. The findings show that both Wall Shear Stress (WSS) and wall pressure rise with higher flow rates and larger sizes of stenosis. Womersley numbers (Wo) significantly dominate the wall pressure, but there are no considerable effects on the peak WSS. The wall pressure profile is shown to be more influenced by the shape of mild contraction than the moderate contraction and right-angle expansion shape (model III). It is also transpired that the WSS of the shape of mild contraction is larger than that of the shape of moderate contraction and right-angle expansion (model III) around the blockage area, and model III shows the greater recirculation length downstream of stenosis. The relative residence time in correspondence with the oscillatory shear index's second peak at the locations of flow recirculation shows the more disturbed flow patterns for model III. Therefore, patients with different models of stenosis will significantly affect atherosclerotic hemodynamics.

Keywords - Computational Fluid Dynamics, Womersley number, Hemodynamic risk factors, Recirculation length, Hemodynamics.

# 1. Introduction

The stenotic vessel's intimal thickening is recognized as the first stage of atherosclerosis. In the majority of nations, atherosclerosis is a major cause of death and a typically dangerous illness. Understanding how blood functions in stenotic vessels is essential because blood components significantly contribute to the atherosclerotic beginning condition. Constriction-induced flow disruptions have been the subject of numerous studies that have contributed to various discussions, analyses, and experimentation. A constricted model is utilized both through computation and experimentation in [1]. According to their findings, the velocity magnitudes are highly dependent on the pulsating flow, especially in the area just after the stenosis. Due to the significance in relation to vascular disorders of the stenosed arterial geometry flow, such as atherosclerosis, which is linked to heart attacks and strokes, numerical studies of its impact are of great interest [2]. Blood's high cholesterol levels lead to the successive accumulation of atheromatous plaque on the arterial inner surface, shortening the flow pathway with the arterial wall's induration [3]. The flow features of turbulence in a stenosed axisymmetric vessel have been studied in [4] with the help of an experimental technique. Kaid et al. [5] have presented a pulsating carotid artery hemodynamics model, encompassing the conditions of normal and stenosis-affected. In this study, blood-connected parameters are examined in relation to flow disturbance and stagnation points.

Ojha et al. [6] have investigated flow pulsation features in a stenosed blood vessel with a blockage ranging from 38 to 75% employing a technique. A turbulent shifting happened in flows for middling blockages due to the formation of waves and vortices moving along the streamwise direction that are released in the layer of high-shear. At Reynolds numbers ranging from 0 to 500, Banerjee et al. [7] have examined the atherosclerotic blood problems with the significant influence of physiological conditions. Their outcomes signify the relation among the potential blood factors. A Newtonian assumption of blood is used in the computation of the steady flow of axisymmetric rigid constrictions by Deshpande et al. [8]. Using Computational Fluid Dynamics (CFD) analysis, the dynamical approach of blood for the constricted carotid artery has been numerically simulated in Hameed et al. [9]. The pressure and velocity profiles oscillate in the post-stenotic area. An inverse potential link for WSS and atherosclerotic intimal thickening has been proposed by Wootton and Ku

[10]. According to Nerem [11] and Chiu et al. [12], endothelial cells lining the arteries display reduced cell consistency and elevated cell division rates near the location of flow reattachment.

A Predictive Surrogate Model (PSM) is employed to forecast the blood hemodynamics in cases of carotid artery stenosis according to Wang et al. [13]. WSS, Oscillatory Shear Index (OSI), pressure, and velocity components are the hemodynamic parameters that are captured by this model. While OSI shows somewhat larger errors, it also creates trustworthy error scales for velocity components and WSS indices. A blood pressure of 500 Pa results in the highest WSS value at the plaque neck, and a blood pressure of 1500 Pa results in the highest WSS value in the vicinity of the plaque root as described in Alagbe et al. [14]. It has also been observed that when the plague size increases, so does the area with exceptionally high WSS values. In different circumstances, the heightened pressure drops linked to the separation of flow at the narrowing minimize the rate of flow, potentially leading to ischemia, necessitating surgical procedures like angioplasty, bypass actions, and stenting as noted by Sherwin et al. [15]. Jeon et al. [16] have examined the effect of the trapezoidal stenosis shape on the flow field of axisymmetric near constriction. They have presented that pressure and shear stress are diversified for various stenosis shapes.

The effect of a stenotic vessel on hemodynamic risk parameters has also been taken into account computationally by Caruso et al. [17], who combined three different geometries, such as parabolic, trapezoidal, and elliptical, with a corresponding stenotic blood vessel in the arterial geometry of the right coronary. According to their research, the geometry with obstruction greatly affects the flow system and WSS, but the lowest region of the vessel is identified as the vital factor that contributes to pressure drop. Liao et al. [18], along with Toufique Hasan and Dipak Kanti [19], have studied how the ratio of constriction of blockage, Womersley number, and Reynolds number affect flow dynamics in stenotic blood vessels. None of these investigations took into account the non-Newtonian blood characteristic. Mahapatra et al. [20] computationally solved pulsatile Navier-Stokes equations with the help of a finite difference approach on a staggered mesh resolution for flow in a channel with the local constrictions of symmetric and asymmetric.

Both physiological and equivalent simple flow pulsations with identical stroke volumes have had their results quantitatively presented by Zendehbudi and Moayeri [21]. The analysis is limited to the axisymmetric Newtonian and laminar blood flow for a rigid blockage wall. Plaque height significantly affects the velocity and distribution of Plaque Wall Stress (PWS) in the vicinity of the plaque, as shown by Amoo et al. [22]. The force associated with blood flow close to the plaque increases with plaque height, increasing the

compression stress. In the artery geometrical realm, Berger and Jou [23] have inspected the detailed discussions of modeling and experiments concerning two and three-dimensional steady and unsteady flows that are most relevant to atherosclerosis. Mittal et al. [24] have used the Large-Eddy Simulation (LES) approach to study the flow pulsation in a constricted vascular model. Eswari et al. [25] have analyzed the behavior of stenosis through arteries with the help of a neural network and multiple linear regressions. In the investigation of the connection between hyperviscosity and physiological conditions, Udupa et al. [26] have found that exercise encourages the separation zone downstream of the stenosis.

The researchers also look at the effects of alternating between resting and exercising, finding a correlation between the rate of transition and the onset of stenosis. Espa et al. [27] have studied the blood flow systems and the hemodynamics related to an abdominal aortic aneurysm estimated in the measurement of an in vitro campaign executed through a laboratory model of an aneurysm with rigid walls and an axisymmetric shape. Padma et al. [28] have displayed the model to meet the flow investigation of Jeffrey fluid arterial blood flow with mild constriction. Kang et al. [29] have examined a velocity-associated procedure to address the solution of unsteady fluid-structure interaction issues in a completely coupled mode through the implementation of the approach of the Eulerian frame and Lagrangian frame. Though the impact of arterial stenosis on hemodynamic parameters has been discussed in [19], the investigation of time-averaged parameters (OSI, RRT), various stenosis models, separation and reattachment points, and Womersley numbers' impact on WSS has not yet been established, that are considered as a research gap in a dynamical flow system, which gives a new idea in biomedical sectors.

Although extensive work has been conducted to analyze the flow pulsation in constricted blood vessels over the last few years, limited investigations have focused on the hemodynamics of blood flow systems due to arterial stenotic models. Thus, the present research is motivated to examine the stenosis models' impact on the pulsating blood flow dynamics for several percentages of area reduction. The current study has also concerned the impact of pulsation, time periods of oscillation, Area Reductions (ARs), flow rate, and Womersley number on the hemodynamic flow pattern to formulate a stenotic arterial blood flow model.

### 2. Materials and Methods

The following various systematic levels connected to CFD are followed in order to provide a convenient numerical investigation for the models of blood flow.

### 2.1. Computational Domain

The numerical investigation utilizes the computational domain of an artery's geometry featuring symmetrical

stenosis, as illustrated in Figure 1. The coordinates (r, z) are assumed for the cylindrical system. In the coordinates, r lies along the radial distance and zlies along the horizontal artery's axis of symmetry. Both the axial  $(u_z)$  and radial  $(u_r)$  components define the overall velocity. In the indicated physical area of the current issue (Figure 1), h represents the blockage radius (the stenosis's tightest section), which R indicates the non-constricted part's radius.

## 2.2. Governing Equations and Boundary Conditions

For a Newtonian fluid undergoing axisymmetric flow that is incompressible and has constant characteristics, the governing equations of flow will become the famous equations of continuity and Navier-Stokes:

$$\rho \nabla \cdot u = 0 \qquad (1)$$

$$\rho \frac{\partial u}{\partial t} + \rho(u \cdot \nabla) u =$$

$$\nabla \cdot \left[ -pI + \mu(\nabla u + (\nabla u)^T) \right] + F \qquad (2)$$

Where the velocity vector is identified by u pressure, which is denoted by the external body forces vector exerted on the system, which stands for blood density, and the dynamic viscosity  $\mu$ .

The following boundary conditions are used in the current simulations:

Imposed parameters at inlet:

$$u_z = \frac{1}{A} \left[ \bar{Q} + P \sin \left( 2\pi \frac{t}{T} \right) \right] \tag{3}$$

$$u_r = 0. (4)$$

- Indicated parameter at outlet: It maintains zero pressure
- Centerline condition: It uses the condition of the axis of symmetry
- Along the wall: It uses a no-slip flow,  $u_r = u_z = 0$ .

In the above case, Arepresents the non-constricted tube area,  $\bar{Q}$  denotes the flow rate of average, pulsating amplitude P, t signifies time, and the pulsation period is T.

## 2.3. Hemodynamic Indices

The hemodynamic parameters concerning the upcoming interpretation are reasonable to accentuate:

To investigate the pulsatile character of blood flow in a stenotic blood vessel, the Oscillatory Shear Index (OSI) is utilized. It is described as

$$OSI = \frac{1}{2} \left[ 1 - \frac{\left| \int_0^T \tau_{wall} dt \right|}{\int_0^T \left| \tau_{wall} \right| dt} \right]. \tag{5}$$

In this case, Trepresents the length of the cycle and  $\tau_{wall}$  denotes the shear stress on the wall.

This index assesses both the leading flow direction and its pulsatility. Its value is zero due to the flow of forward during a cycle, while 0.5 represents a purely oscillating flow with a zero  $WSS_{mean}$ ..

Relative Residence Time (RRT) can be defined as

$$RRT = \frac{1}{(1 - 20SI)TAWSS} \tag{6}$$

The RRT parameter can be flexuously related to accurately calculating how long particles will spend in different regions of the walls of the artery.

#### 2.4. Numerical Solution

All research tasks related to modeling, meshing, and computation studies have been performed using COMSOL Multiphysics 5.2. The governing equations in this investigation are solved with the help of the finite element approach. The finite element method subdivides the domain into a finite number of elements to predict the structural characteristics.

For the simulation, the implicit Backward Differentiation Formula (BDF) was selected using the solver technique.  $10^{-4}$  is chosen as the convergence criteria. A time interval of  $\Delta t = 0.003s$  is fitted to execute the simulation. The offered mathematical model has been accommodated on the surface of the CPU (Intel Core i7, 8th Gen 8700 with base frequency 3.20 - 4.60 GHz).

## 2.5. Grid Independence

The independence of computational solutions is necessary due to the lengths of the blood vessel's inlet and outlet relative to the blockage. A number of computational approaches have been conducted to determine the appropriate lengths so that the results of the input and outflow lengths become unbiased. It is suggested that 5D and 22D lengths pre-stenosis and post-stenosis from the throat of the constriction, respectively, are requisite.

The mesh sensitivity interpretation has been accomplished to optimize the grid numbers. According to the grid, the outcomes will not alter in any way when the number of cells changes. Seven various grid sizes, such as extra coarse, coarser, coarse, normal, fine, finer, and extra fine meshes, have been deliberated sequentially. It has been unearthed that the last two grid sizes are almost identical.

Hence, for expediency investigation, the finer mesh with 158401 elements and 256852 degrees of freedom has been adopted to simulate the outcomes in the numerical computation. The software uses the finite element method for the grid resolution. Extensive investigations are conducted with several mesh sizes for various axial lengths from the stenosis center, as shown in Table 1.

| Table 1. Gr | id independe | ency to | test for mean flow i | rate, | Q = 258 | [ml/min], | Wo = 7.7 | 5, AR = 55% | , stenosis shaj | pe model I |
|-------------|--------------|---------|----------------------|-------|---------|-----------|----------|-------------|-----------------|------------|
|             |              |         |                      |       |         |           |          |             |                 |            |

| Mesh         | Time Step  | No. of Elements | Number of Degrees<br>of Freedom | Dimensionless maximum velocity at the post-stenotic region |      |       |
|--------------|------------|-----------------|---------------------------------|--|------|-------|
|              |            |                 | of Freedom                      | 1.2D   | 1.7D | 2.5D  |
| Extra coarse | t/T = 0.25 | 6283            | 12334                           | 4.40   | 4.35 | 4.11  |
| Coarser      | t/T = 0.25 | 12091           | 22039                           | 4.49   | 4.38 | 4.18  |
| Coarse       | t/T = 0.25 | 24332           | 42316                           | 4.51   | 4.42 | 4.259 |
| Normal       | t/T = 0.25 | 38987           | 65962                           | 4.51   | 4.42 | 4.26  |
| Fine         | t/T = 0.25 | 75289           | 122551                          | 4.51   | 4.42 | 4.27  |
| Finer        | t/T = 0.25 | 158401          | 256852                          | 4.52   | 4.42 | 4.27  |
| Extra fine   | t/T = 0.25 | 334751          | 537874                          | 4.52   | 4.42 | 4.27  |

#### 2.6. Methodology Validation

As the first stage in our study, the computational solutions are compared with the experimental and numerical investigations for the case of pulsatile flow.

# 2.6.1. Validation of Pulsatile Flow for the Numerical Computation

The current numerical simulations are verified using a variety of computational and experimental outcomes involving conformable laminar flows of pulsation through a stenotic tube in order to investigate the results. Figure 2 shows the waveform of the present pulsating flow, which is  $4.3\pm2.6$  ml for a duration of 345 ms. Similar to deodorized kerosene, the fluid under consideration has a density of  $755kg/m^3$  and a viscosity of  $0.00143N.s/m^2$ . Since blood is said to be

Newtonian, both kerosene and blood will have uniform flow characteristics for the identical Reynolds number. The input pulse is characterized by a sinusoidal waveform for an average Reynolds number equal to 575, with the consideration of maximum and minimum Reynolds numbers ranging from 230 to 930. A Womersley numeric value of 7.75 is taken for this pulse. A comparison of present outcomes between the measured (Ojha et al. [6]) and computed (Banerjee et al. [7]) axial velocity profiles at the time interval,  $T_1 = 0.175$ , is illustrated in Figure 3 during D, 2.5D, and 4.3D distances from the stenosis throat. The figure shows an excellent correlation between predicted outcomes and the aforementioned literature findings across the time level and locations. The verifications guarantee the code's ability to forecast.

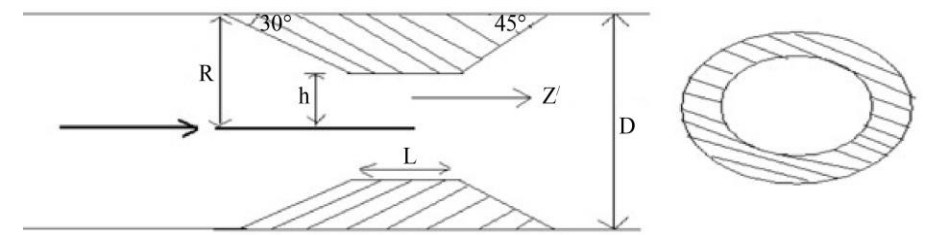


Fig. 1 Simulations were conducted using stenotic geometry, in which L = 1.5 mm, diameter is 5.0 mm, and Z/is the dimensionless distance

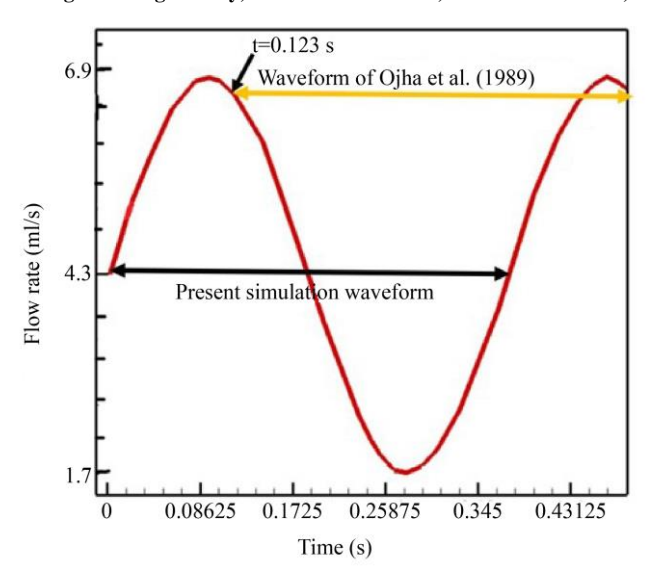


Fig. 2 The typical flow rate of volumetric employed in the numerical computation aligns with that of Ojha et al. [6]

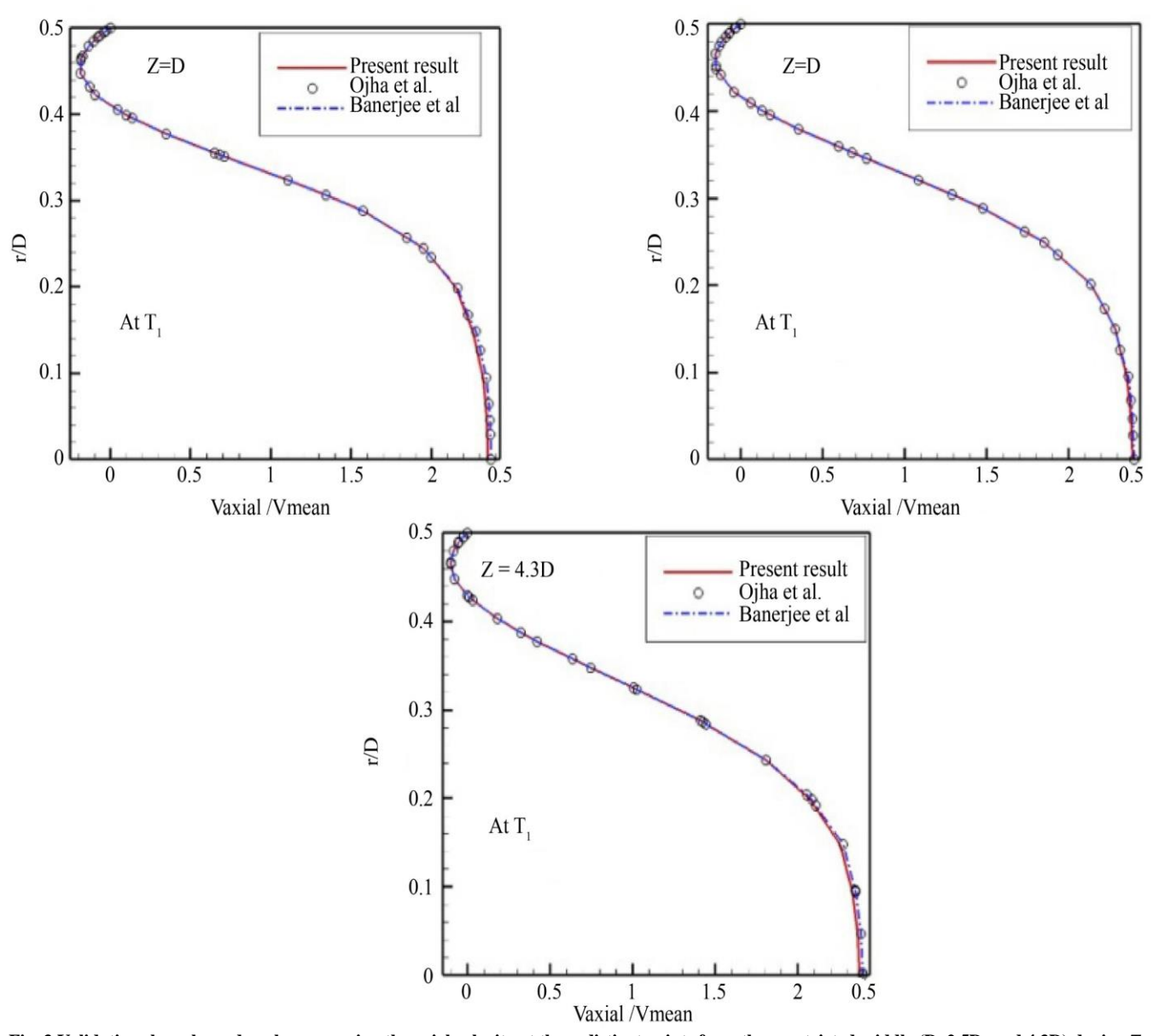


Fig. 3 Validations have been done by measuring the axial velocity at three distinct points from the constricted middle (D, 2.5D, and 4.3D) during  $T_1$ = 0.175

## 3. Results and Discussion

Initially, the current code has been validated using simulations of the pulsatile flow problem. Next, three various stenosis shapes with three ARs are considered for examining the impact of stenosis shape, flow rate, constriction ratio, post-stenotic recirculation length, OSI, RRT, and the numeric value of Womersley on the flow fields around and post-stenotic zones of stenosis. Three shapes of stenosis models are displayed in Table 2.

# 3.1. Stenosis Shape's Impact on the Blood Flow

The impact of different stenosis models on the hemodynamic flow field at and post-stenotic areas is investigated by performing simulations based on the grid resolution explained in the earlier grid independence assessment. Several ARs (40%, 55% and 65%) are assumed for the predicted simulation.

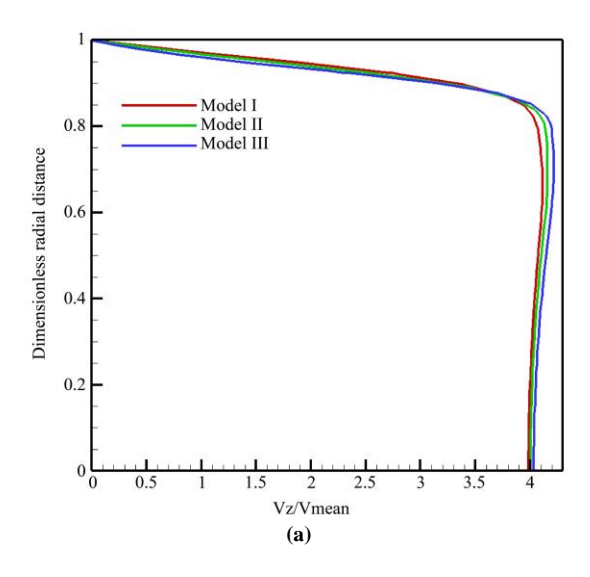
The stenosis forms taken into consideration in this investigation are displayed in Table 2. The validated computation uses Model I, featuring a mild contraction and mild expansion, containing the angles of  $30^{\circ}$  and  $45^{\circ}$ . Model II exhibits the identical mild contraction and moderate expansion with  $45^{\circ}$  and  $60^{\circ}$  and finally, Model III is adopted with the moderate contraction and right angle expansion of  $60^{\circ}$  and  $90^{\circ}$ .

Table 2. Three stenosis shape models in the present study for 40%, 55% and 65%

| Stenosis model  | Stenosis shape |  |  |  |  |
|---|----------------|--|--|--|--|
| Model I: Mild contraction and Mild expansion              | 300 450        |  |  |  |  |
| Model II: Mild contraction and moderate expansion         | 450 600        |  |  |  |  |
| Model III: Moderate contraction and right-angle expansion | 600 900        |  |  |  |  |

# 3.2. Axial Velocity Profiles within the Flow Field

The flow field may be dominated by the presence of a blockage shape in an artery, as displayed in Figure 4 for a 55% area reduction, Wo = 10, and Q = 258 [ml/min]. The distributions of axial velocity for three stenosis models at maximum flow rate have been presented in Figures 4(a) and 4(b), corresponding to the throat and post-stenotic region, respectively. It is exposed that the maximum dimensionless velocity at the stenosis location is around 4, and the poststenotic region exceeds 4. Flow speeds up and reaches its maximum velocity, as seen in Figure 4(a). In contrast to the arterial width, the distribution of velocity turns out to become flat and indicates a thin layer at the boundary. It was also detected that the maximum axial velocity may not happen on the centerline in all cases. Peaks in the velocity profile appear symmetrically at a dimensionless radial distance of 0.80 due to this case. Beyond the blockage area, the flow diminishes in speed, and the boundary layer may separate, as stated in Figure 4(b). It is notable that model III gives a higher velocity than the others, as presented in Figure 4. The distribution of velocity across the blockage site is disturbed by unsteady flow. The arterial neck gives a considerably flattened velocity distribution, and a recirculation zone appears downstream of the stenosis.



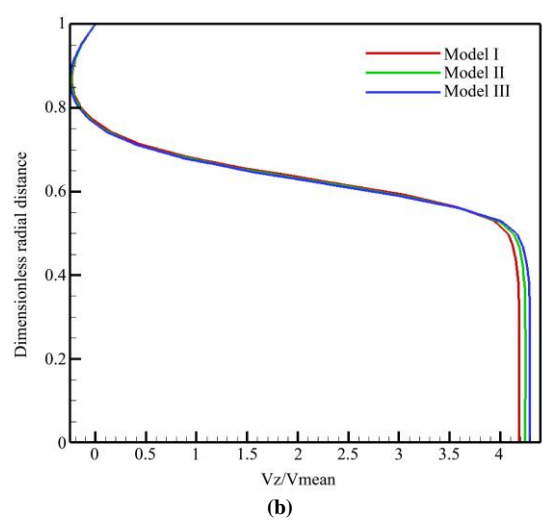


Fig. 4 Instantaneous axial velocity profiles at an area reduction of 55%, Q = 258 [ml/min], Wo = 10, (a) throat of the stenosis and (b) 0.5D downstream from the center of the stenosis

## 3.3. Effect of Stenosis Shape on Wall Pressure Distribution

One crucial indicator of the degree of obstruction that might result in life-threatening circumstances if not properly recognized and monitored is the pressure drop that occurs as a result of stenosis. Figure 5 displays the wall pressure at a maximum flow rate (t/T=0.25) along the artery walls with the three stenosis model shapes for the Area Reductions (ARs) of 40% and 65% for Figures 5(a) and 5(b). The wall pressure is portrayed over the AR for the three stenosis model shapes of the arterial vessel (Figure 5(c)), depending on the data in the figure. The enormity of the wall pressure across the blockage grows as the ARs also grow.

Stenosis with moderate contraction (Model III) has a greater pressure drop than those with mild contractions. It also suggests that the wall pressure is truly dependent on the shape of the stenosis. Though the increasing rate is slow, the highest wall pressure is noticed in model III compared to the other two stenosis shapes. It is investigated that the wall pressure is dependent on the shape of the stenosis. The wall pressures are exhibited for the maximum flow rate (t/T = 0.25) in the figure.

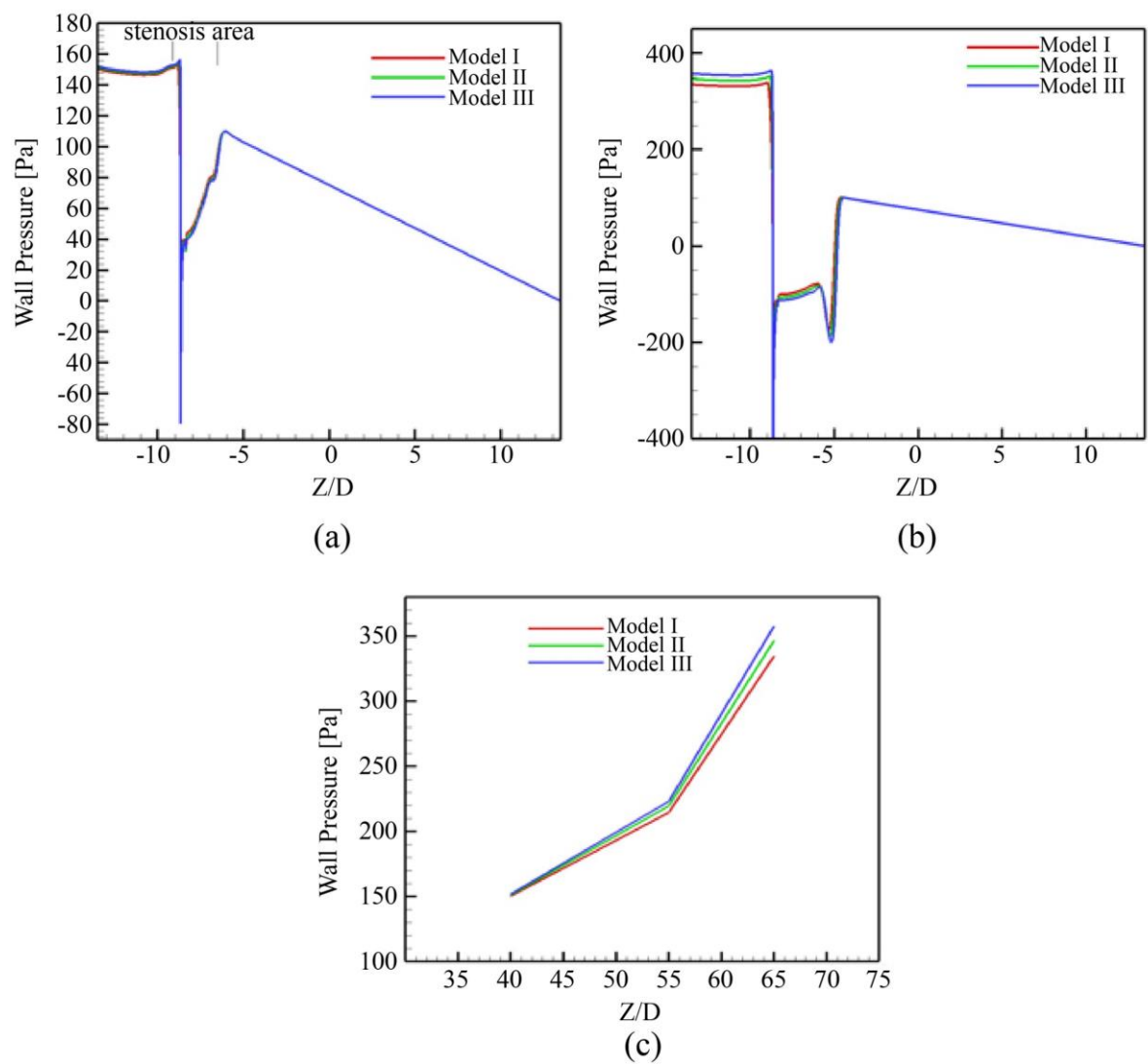


Fig. 5 Wall pressure at maximum flow rate (t/T=0.25) for (a) 40%, Wo = 10, flow rate = 258 [ml/min] (b) 65%, Wo = 10, flow rate = 258 [ml/min] (c) AR vs wall pressure, Wo = 10, flow rate = 258 [ml/min]

### 3.4. Stenosis Models' Impact on WSS

The aim of this discussion is also to investigate the effect of stenosis shape on the hemodynamic flow characteristics, which indicates the accumulation of lipids within vessels. All three types of stenosis shapes, with their slopes and curvatures, are distinct. Both the degree of blockage and the stenosis model's angle have a significant influence on WSS. As demonstrated in Figures 6(a) and 6(b), stenosis model II (mild contraction and moderate expansion) has a higher WSS for 40% and 65% area blockage at peak flow rate, which is also visible in the plotted graph. This elevated WSS is clinically linked to the atherosclerotic plaque's rupture and instability, potentially resulting in heart attacks and strokes. Additionally, it should be noted that the figure's depiction of the stenosis angle's impact on WSS is more noteworthy. The magnitude of WSS is portrayed for three stenosis shapes with ARs and is displayed in Figure 6(c). In model II, endothelial cell injury may be triggered by a shear force of 37 Pa. As shown in the image, endothelium cells are susceptible to injury at every constriction of 40%, 55% and 65% in model II. Nonetheless, in the other two forms, the endothelium cells remain intact at the 40% stenotic level. When the severity is increased to 55%, it results in a maximum shear stress of approximately 65 Pa in model II, surpassing 45 Pa for the stenosis model I, and in stenosis model III, it is around 30 Pa. For 65% severity, the highest shear stress (97 Pa) is observed solely in model II. This value is about 72 Pa for model I and is about 40 Pa for model III. A low WSS value environment in model III enhances the permeable feature in an endothelium cell, facilitating the absorption and buildup of low-density lipoprotein in the arterial wall of blood. As a result, blood clots develop, prompting platelets to repair the injured region, thereby making the arterial obstruction worse.

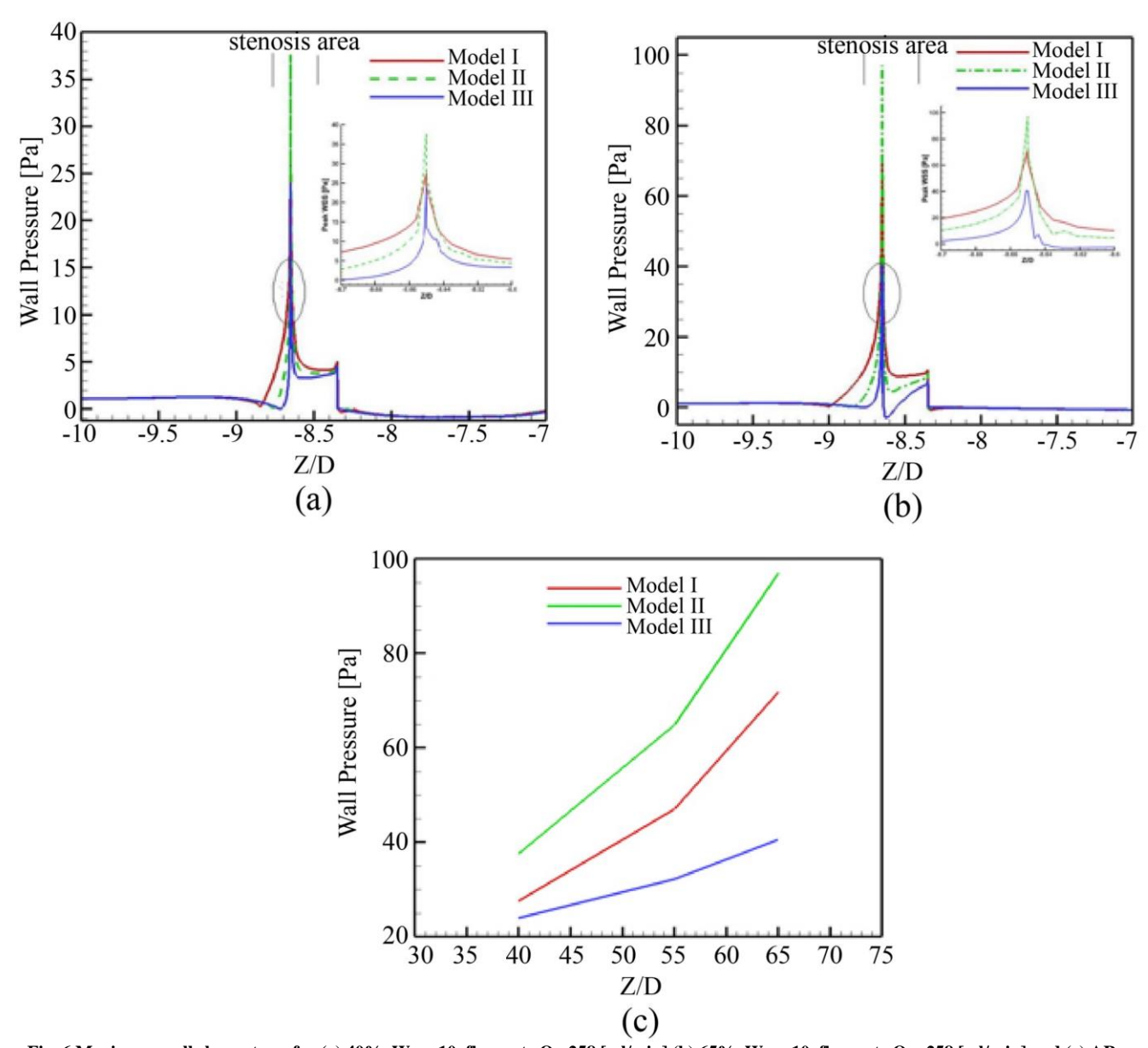
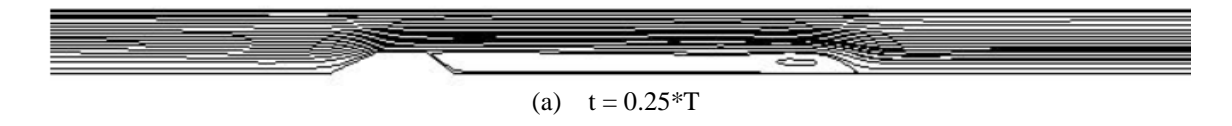


Fig. 6 Maximum wall shear stress for (a) 40%, Wo = 10, flow rate Q =258 [ml/min] (b) 65%, Wo = 10, flow rate Q = 258 [ml/min] and (c) AR vs maximum wall shear stress, Wo = 10, flow rate, Q = 258 [ml/min]

# 3.5. Generated Streamlines, Wall Pressure, and WSS due to Q = 258 [ml/min], Wo = 10

Due to the flow being unsteady, the flow field as a timevarying approach is more pertinent for practical biomedical applications. As seen in Figure 7, with 55% area constriction, the generating streamlines of the flow indicate a significant change in every aspect during a cardiac cycle. The streamlines easily traverse the obstruction flow field, creating a vortex closely adjacent to the area at the downstream site of constriction. The locations for separation and reattachment are determined by the position of inflection of the wall's curve. As can be seen in Figure 7(a), due to t/T=0.25, the fixated recirculation enlarges and eventually becomes broader as the flow increases to the highest flow rate. At t/T=0.5, the momentary flow rate aligns with the average rate for a complete flux's deceleration, resulting in the vortex spreading out more in the distant location.



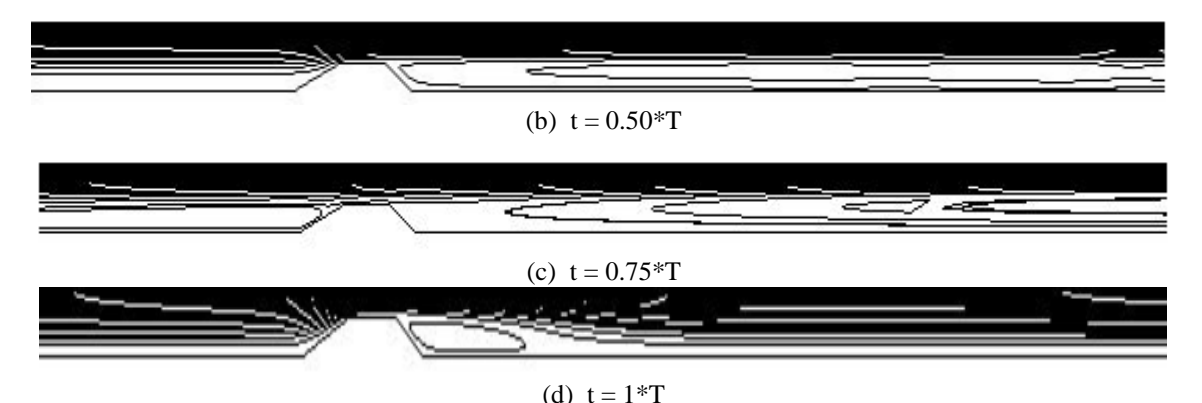


Fig. 7 Flow streamlines for flow rate, Q = 258 [ml/min], Wo = 10,55% stenosis model I

At t/T = 0.75, as the flow reaches its zero net flux and correlatively low speeds, the leftovers of the unhitched vortices occupy a majority of the constricted flow area, both far from the throat and close to it. When the duration increases even more until t/T = 1.0, the following cycle proceeds, and the flow reproduces itself. In Figure 8, the wall pressure for three stenosis models of 55% blockage is displayed at

different instants of time. The peak pressure is not in phase with the peak flow rate (t/T = 0.25), at the phase-lag occurs around the maximum acceleration point of the mass flow profile (t/T = 1.00), the maximum deceleration (t/T = 0.50) for all stenosis models are in negative zone and at the minimum flow rate (t/T = 0.75) wall pressures are about to zero for all the cases.

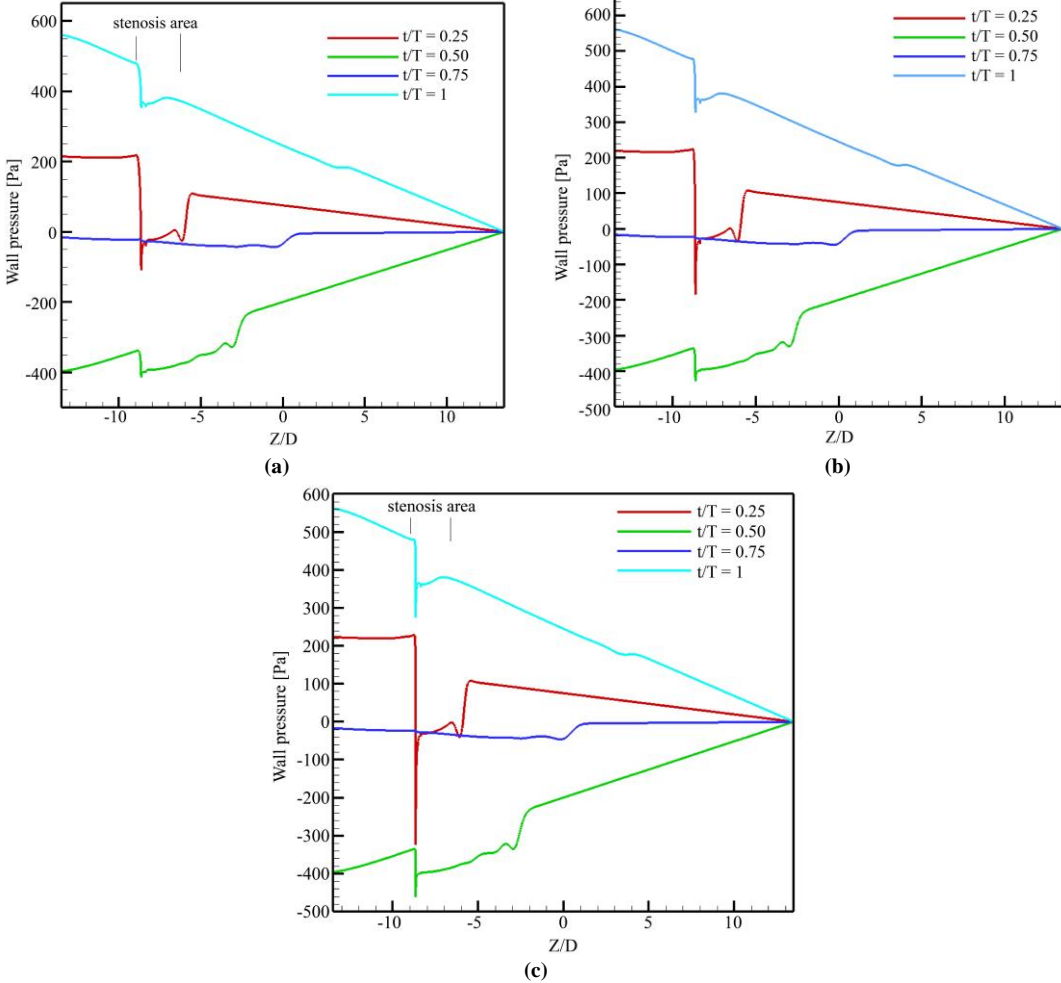


Fig. 8 Wall pressure at time steps t/T = 0.25, t/T = 0.50, t/T = 0.75, t/T = 1, Wo =10, flow rate Q = 258 [ml/min], AR = 55%, for (a) Stenosis model II, (b) Stenosis model III.

WSS is investigated at several time instants throughout the whole cardiac cycle, as displayed in Figure 9, with a 55% blockage intensity as a key hemodynamic factor in assessing atherosclerotic development. The constricted neck experiences the greatest WSS. At the cycle's peak flow rate or t/T = 0.25, the WSS is at its greatest. A vortex is created by the differential in WSS between the areas upstream and downstream. The maximum WSS at t/T = 0.25 is 2.63 and

2.15 times larger than the values at t/T=0.5 and 1, respectively for Figure 9(a) (model I); and for Figure 9(b) (model II), the peak value of WSS is 2.69 and 2.12 times higher; and further, for Figure 9(c) (model III), it is 1.94 and 1.69 times bigger than that for t/T=0.50 and t/T=1, respectively. When the overall flux is zero at t/T=0.75, it signifies a considerable increase in WSS at the location of the constricted neck for three cases.

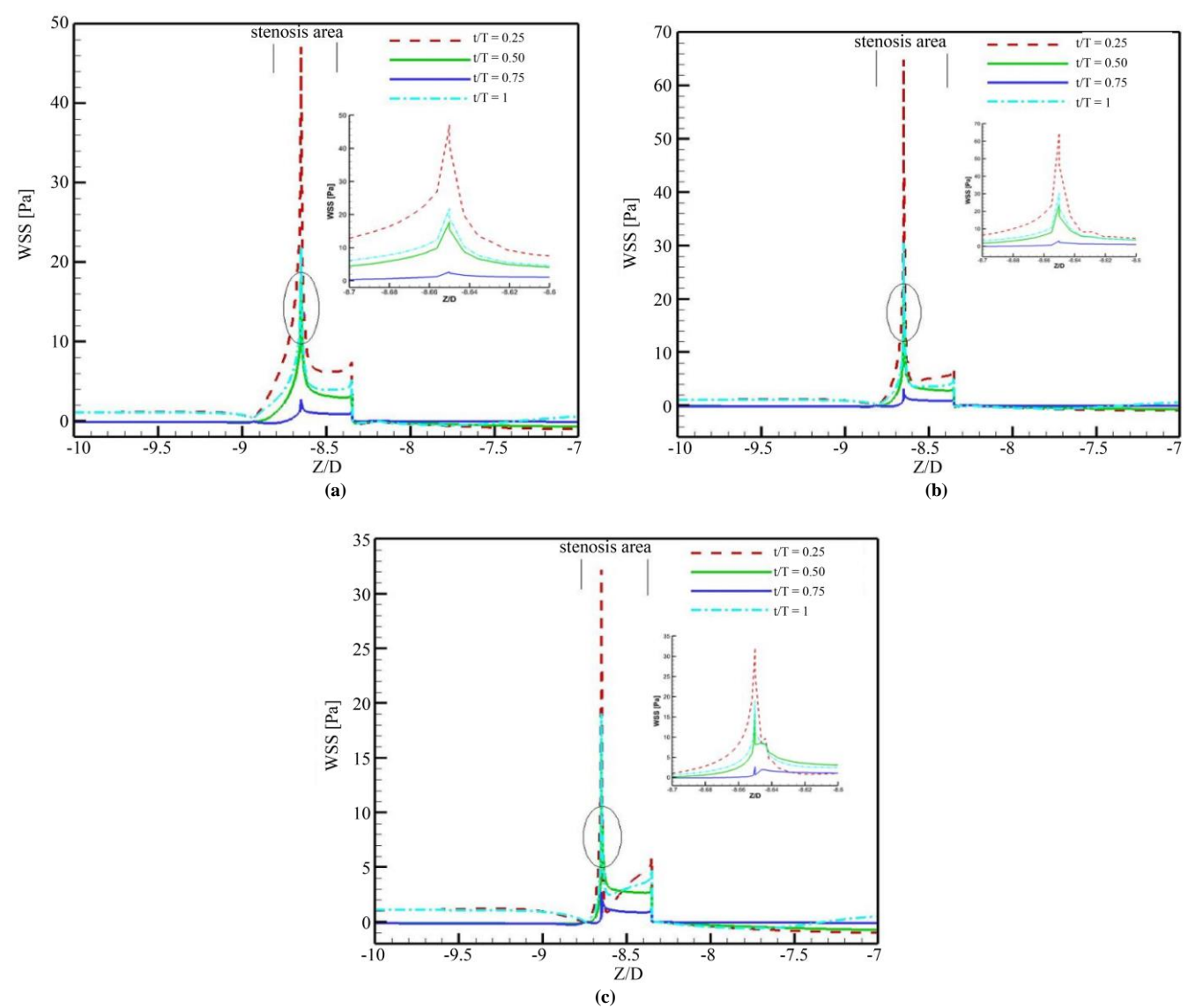


Fig. 9 Wall shear stress for the time instants of (t/T = 0.25, t/T = 0.50, t/T = 0.75, t/T = 1), Wo =10, flow rate Q = 258 [ml/min], AR = 55%, for (a) Stenosis model II, (b) Stenosis model III.

#### 3.6. Effects of the Flow Rate (Q)

The flow rate is known to be a critical factor in the flow field characteristics within a narrowed artery during pulsating flow. This part discusses how the flow rate affects the pulsation of the flow field. A narrowed artery exhibiting 55% area reduction, Wo or Womersley numeric value is 10,

average flow rate (Q) = 258 [ml/min], and 300 [ml/min] and 450 [ml/min] will be observed for model I. The momentary streamlines for sinusoidal pulsatile flow at flow rates, Q = 300 [ml/min] and 450 [ml/min], are exhibited in Figure 10(a) and Figure 10(b), respectively. Mentioning the streamlines in Figures 7, 10(a), and 10(b) at t/T = 0.25 or the peak flow point,

the connected vortex remains elevated at flow rate, Q=300 [ml/min], and increases in size at flow rate, Q=450 [ml/min]. The associated vortex expands in size as the flow diminishes following the peak flux. Once more at t/T=0.5, lower vorticity is noticed due to Q=258 [ml/min] compared to Q=300 [ml/min] and Q=450 [ml/min]. The remains of the split vortices retain both the proximal and distal to the throat at t/T=0.75 during the zero net flux of flow rate. Nonetheless, Q=258 [ml/min] exhibits the lowest vortex. At the maximum acceleration point (t/T=1), the vortex is larger during Q=450

[ml/min] compared to Q = 258 [ml/min] or Q = 300 [ml/min]. In Figure 11 (a), the magnitude of the wall pressure is greater for the flow rate, Q = 450 [ml/min] during peak systole or t/T = 0.25, corresponding to the other two flow rates. The wall pressure for flow rate, Q = 450 [ml/min], is 1.51 and 1.37 times larger than that of other flow rates. Due to the fact that the peak WSS distribution at t/T = 0.25 near the stenosis throat during the highest flow rate surpasses those at different time levels, and is displayed in Figure 11 (b) for conciseness.



Fig. 10 Streamlines for stenosis model I for (a) flow rate, Q = 300 [ml/min], (b) flow rate, Q = 450 [ml/min] of 55% stenosis at time intervals (t/T = 0.25, 0.50, 0.75, 1)

As flow rates increase, the peak WSS rises monotonically. It is also important to remember that when the flow rate rises, the maximum WSS location tends to move just before stenosis. The WSS for Q=450~[ml/min] is 1.63 and 1.43 times greater than that for Q=258~[ml/min] and 300 [ml/min]. Again, for Q=300~[ml/min] and 450 [ml/min], the Wall Shear Stress (WSS) downstream of the constriction does

not seem to recuperate its untroubled upstream values as it does for  $Q=258\ [ml/min]$ . This is because the recirculation zone has grown in size to accommodate the higher flow rate. In summary, disparities in flow rates can have a terrible impact on the flow system. The peak WSS might increase significantly with a larger flow rate.

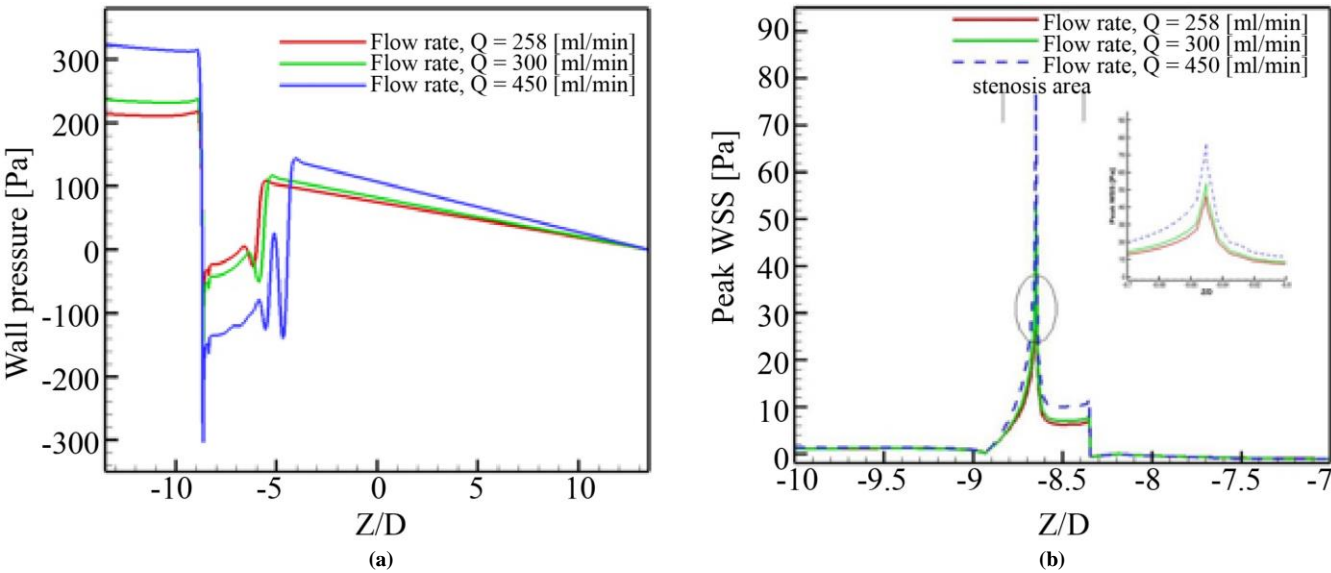


Fig. 11 Distributions of (a) Wall pressure, and (b) peak wall shear stress during peak systole due to 55% blockage and Wo = 10 at several flow rates (O = 258, 300, 450 [ml/min]) for model I.

# 3.7. Womersley Number's Impact

Detailed observations of the flow areas for a range of Womersley numbers are made without altering the stenosis intensity and flow rates. The simulation takes into account 6, 7.75, 10, and 12.5 as Womersley numbers, keeping the flow rate, Q, fixed to 258 [ml/min] and the size of stenosis of 55% for model I. Figure 12(a) indicates the wall pressure for various Womersley numbers, and it is observed that the wall pressure increases with the increase of Womersley numbers. The wall pressure for a maximum flow rate or the time, t = 0.25\*T, is attached with a Womersley number of 12.5, and it is followed by 10, 7.75, and 6. Figure 12(b) displays the instantaneous wall shear stress distribution during the peak flow time (t/T = 0.25) for the Womersley numbers 6, 7.75, 10,

and 12.5. The varying flow characteristics downstream of stenosis under varied Womersley numbers are also investigated, and it is observed that for the two cases (Wo =10 and 12.5), an oscillation in the shear stress is noticed in the downstream region. It can be observed that the peak values of momentary wall shear stress are not significantly affected by the variation of the Womersley number. In contrast to the Womersley numbers of 6 and 7.75, the WSS downstream of the blockage for Wo = 12.5 regains a comparable value as that of the obstruction upstream more quickly than for Wo = 10. The WSS recovery procedure is extremely slow for low Womersley values. The figure makes it clear that Wo values have no great impact on peak WSS. However, there has been a significant shift in the lowest WSS values.

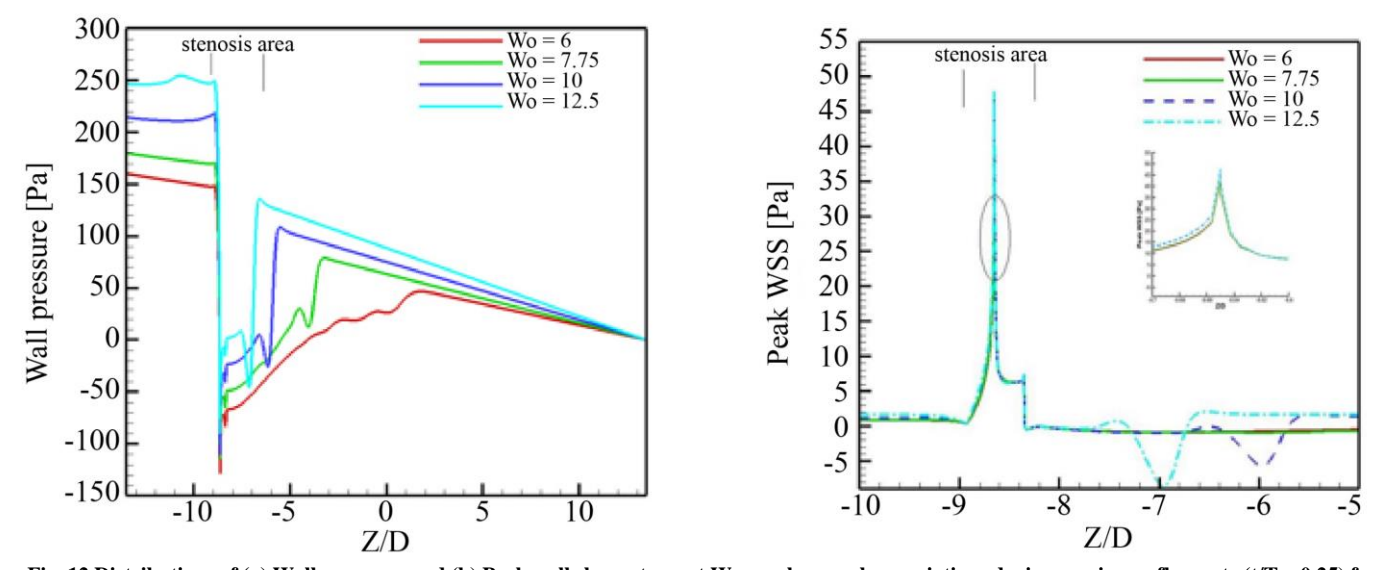


Fig. 12 Distributions of (a) Wall pressure, and (b) Peak wall shear stress at Womersley number variations during maximum flow rate (t/T = 0.25) for model I with mean, Q = 258[ml/min], stenosis = 55%.

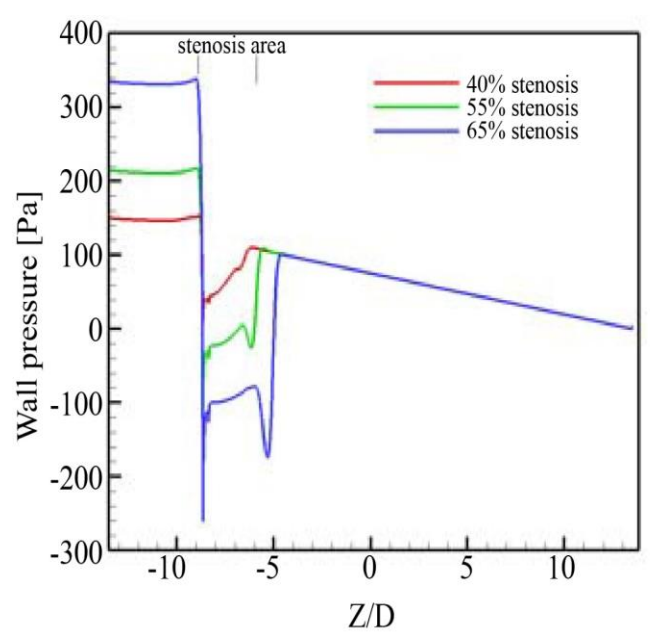
## 3.8. Stenosis Size's Impact

In a narrowed artery, the flow area is significantly influenced by the degree of stenosis. This section will examine how the flow changes for model I as the stenosis size changes. The predicted numerical solutions for sinusoidal fluctuated flow are compared for three stenosis sizes of 40%, 55% and 65%. The flow rate, Q, is set at 258 [ml/min] and the Womersley value is 10.

As the volume of blockage increases, the pulsating flow area becomes increasingly problematic. Once more, Figure 13(a) shows the wall pressure during peak systole (t/T=0.25), for the sake of analysis appropriateness. The wall pressure value for 65% blockage is increased by 2.25 and 1.57 times for another blockage size.

during peak flow is shown in Figure 13(b). The WSS has a great impact on the flow due to the 65% severity, particularly where the stenosis is located. In the case of 40% blockage, the maximum WSS value is 29 Pa, and the post-stenotic WSS quickly returns to the pre-stenotic WSS level because of minor disruptions caused by the aforementioned constriction that are not apparent with more severe stenosis. When compared to equivalent levels of WSS at 40% and 55% blockage densities, the maximum WSS at 65% blockage is 2.61 and 1.52 times larger. The value of the highest wall shear stress rises monotonically with increasing constriction severity. It is clear from the discussion above that the extent of severe narrowing results in a more intricate flow area. As the obstruction intensity increases, the wall pressure and WSS often rise as well.

The distribution of peak WSS at several blockage sizes



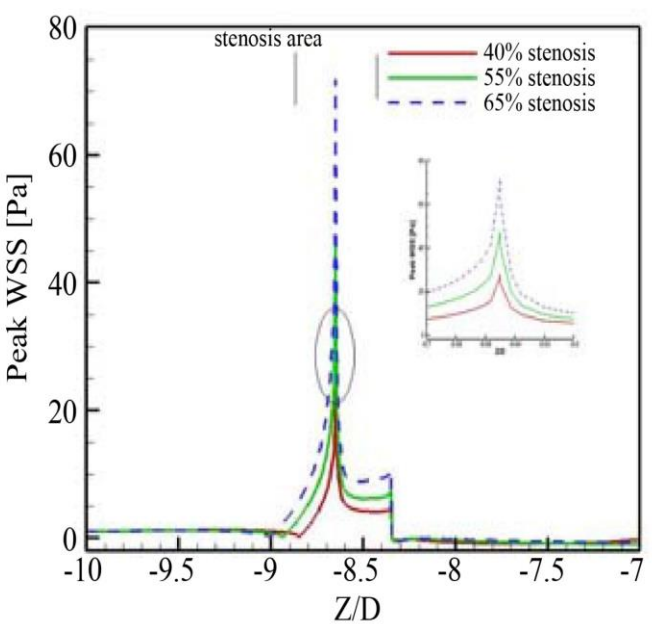


Fig. 13 Distributions of (a) Wall pressure, and (b) Peak WSS for different stenosis sizes at mean Q=258 [ml/min], Wo = 10, t/T = 0.25 for model I.

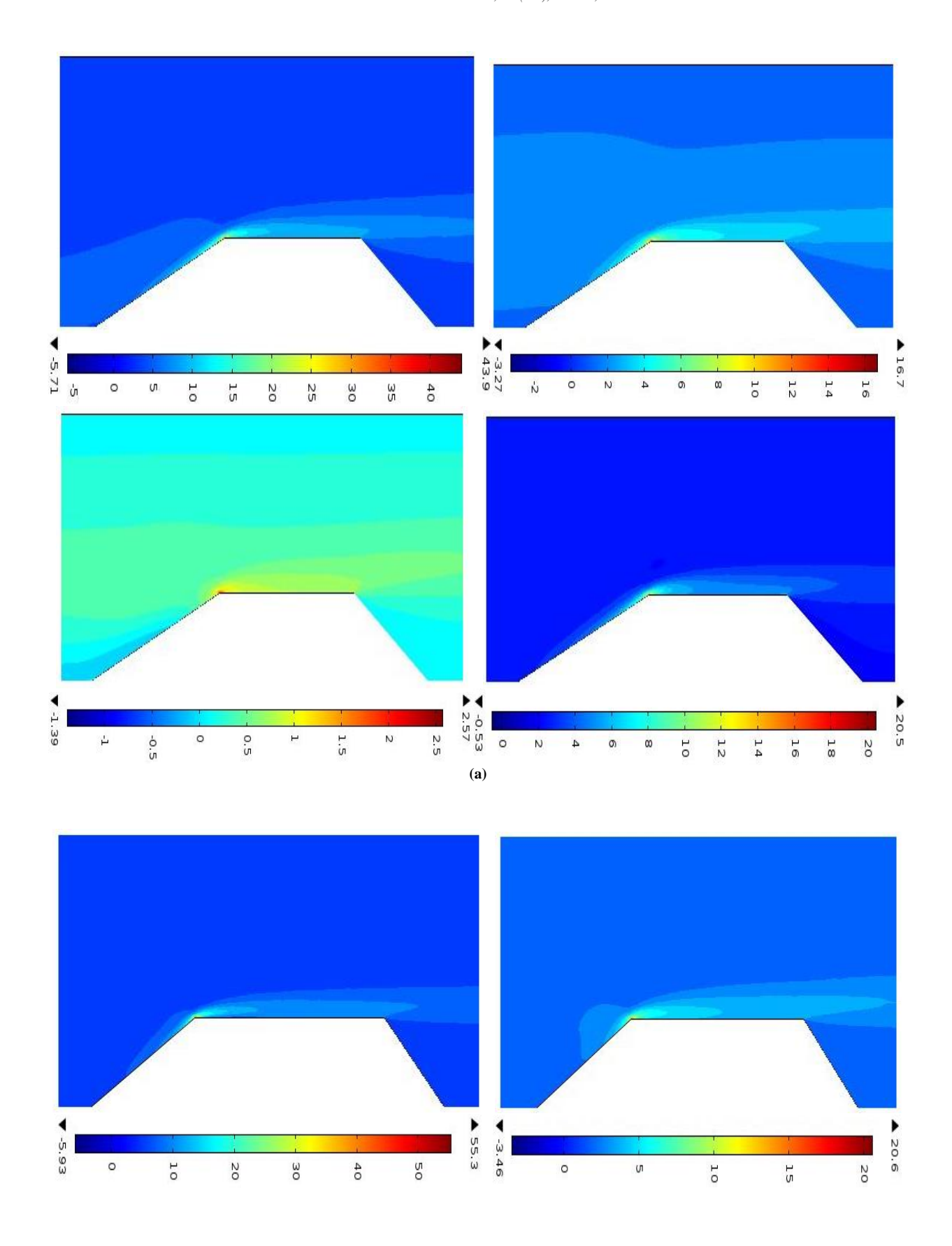
# 3.9. WSS Contours and Post-stenotic Separation Zones for the Investigated Stenosis Shapes

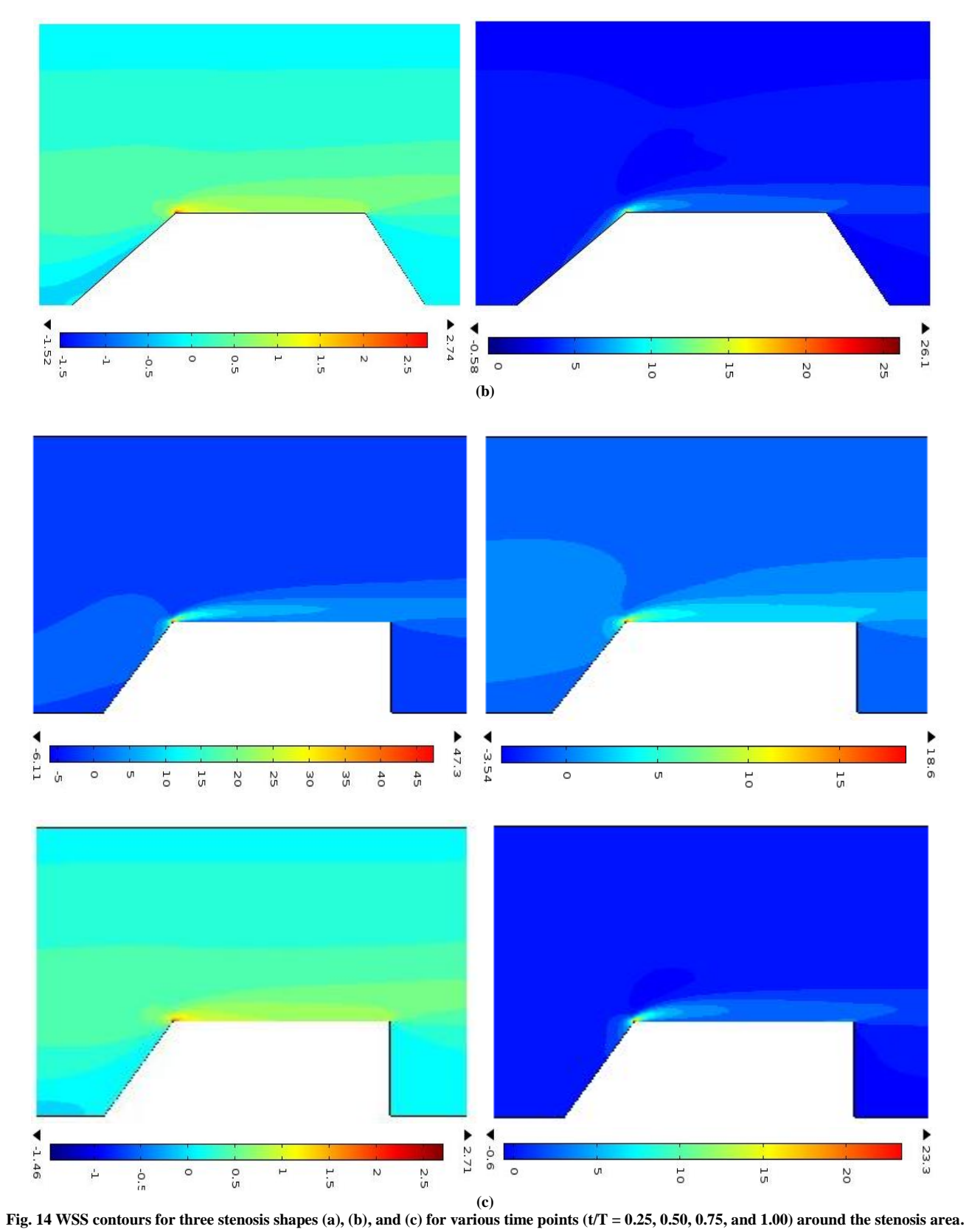
The comparison of WSS contours around the blockage area at 55% constriction of the area is discussed for various time steps (t/T = 0.25, 0.50, 0.75, 1) in one cardiac cycle (Figure 14) for three stenosis models, keeping the flow rate, Q = 258 [ml/min] and Wo = 10. Peak wall shear stress occurs at the throat of stenosis, which is compatible with observations repeatedly reported above.

The magnitude of wall shear stress is the highest at the maximum flow rate (t/T = 0.25) in the whole cycle. Comparing the value at a certain time level for different stenosis shapes imparts that the WSS value decreases as flow moves towards the minimum flow phase (t/T = 0.75), and then it increases; the largest WSS appears in model II among them. Negative wall shear stress area, commencing the occupancy

of flow reversal, develops axially larger from t/T=0.25 to 0.75 and can stretch as far as the whole post-stenotic, though it softly reduces from t/T=0.75 to 1.0. Figures. 15(a) and 15(b) display the axial variation of the fugacious Wall Shear Stress (WSS) at several time instants of the cardiac cycle, in the downstream location immediately following the stenosis, respectively.

From Figure 15(a), it is quite obvious that the recirculation length increases from t/T = 0.25 to 0.75 and then decreases from t/T = 0.75 to 1.0. However, the size of the recirculation zone in the downstream area for the cases studied here is longer in the stenosis model III compared with the others. Further, it is concluded that the moderate contraction shape has a greater recirculation zone than the mild contraction.





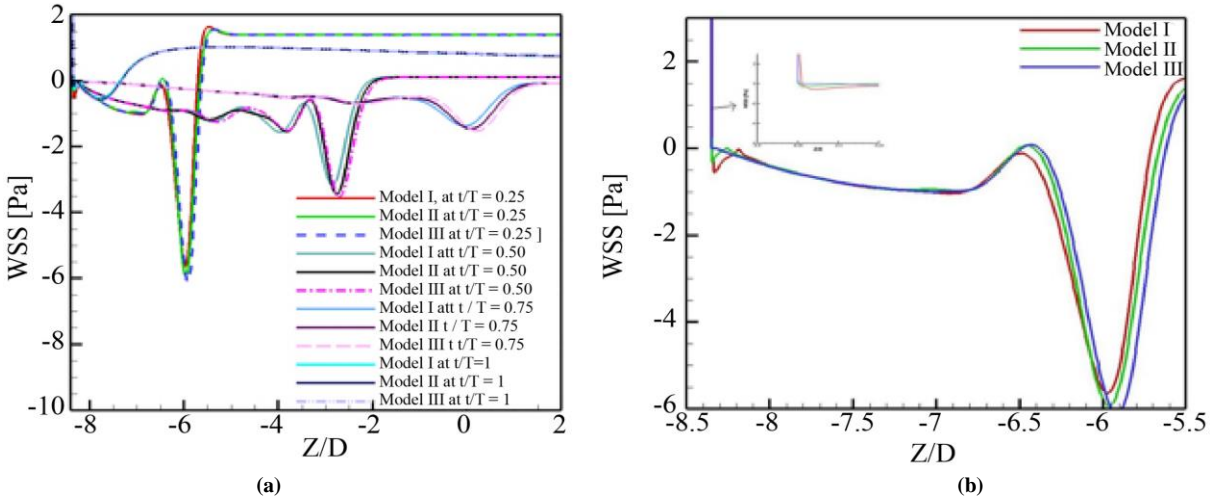


Fig. 15 WSS at post-stenotic for three shapes: (a) At various time steps ,and (b) At peak systole (t/T = 0.25) for an enlarged view.

## 3.10. Stenosis Shape's Impact on Hemodynamic Parameters

In Figure 16 (a), the OSI distributions are shown introductorily with a view to obtaining the time-averaged results with the highest apex succeeded by an additional maximum apex in every instance. The flow separation point is indicated by the first peak, and the flow reattachment point, as TAWSS drops to zero, is indicated by the second peak. The figure expressly suggests that the position of time-averaged separation and reattachment points is greatly dominated by the stenosis models. For illustration, flow separation happens at z = 4.55\*D, z = 4.69\*D, and z = 4.74\*D for model I, model II, and model III, respectively, measured from the artery beginning, whereas the corresponding points of flow reattachment are placed at z = 9.82\*D, z = 10.01\*D, and z =10.13\*D, respectively. However, the first peak's OSI, which approaches the maximum values close to 0.5, that is, 0.23 for model I, 0.42 for model II, and 0.49 for model III, is significantly influenced by the geometry of the stenosis. As noted by Gallo et al. [30]. OSI values close to 0.5 impart areas in which the cells of the endothelial layer distract alignment, hence impairing the endothelium's permeability. Notably, the aforementioned features activate the time-averaged flow, but in the dynamic scenario, the reattachment point and flow separation point vary throughout the pulsation cycle.

Conclusively, Figure 16(b) shows the distributions of RRT. The RRT distributions' peaks align with the OSI distributions' peaks at which OSI approaches 0.5, so that achieving extraordinarily elevated RRT magnitudes (in theory RRT  $\rightarrow \infty$  whenOSI  $\rightarrow$  0.5). Identical RRT tops are observed in the downstream region of stenosis in a different investigation by Huang et al. [31] and Kelidis et al. [32], aligning with the reattachment point at which OSI equals 0.5. Such elevated RRT steps are significantly higher than physiological steps detected in healthy people's unblocked arteries, as is customary RRT<18 (Soulis et al. [33]; Gallo et al. [30]). Due to the lengthy particle residence period, lipids may accumulate in the post-stenotic region, which could create a second, third, etc.

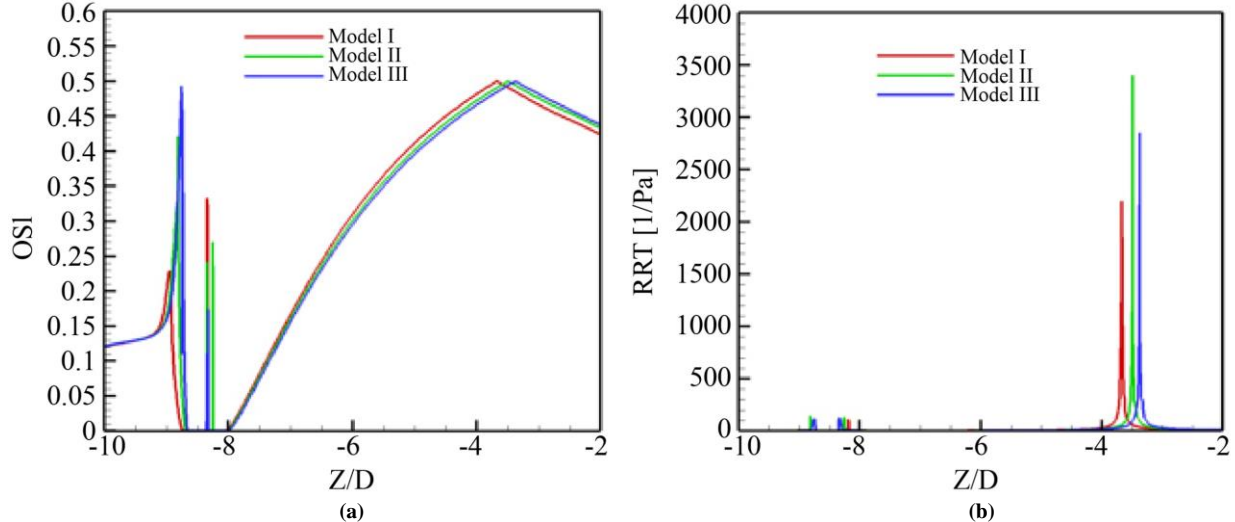


Fig. 16 (a) OSI, and (b) RRT distributions along the arterial wall for all models.

## 4. Conclusion

In order to evaluate the impact of blockage shapes on hemodynamic critical factors, this research offers a numerical investigation of pulsating flow via a stenotic artery. COMSOL Multiphysics' FEM solver is used to model and solve the pulsating flow. Three distinct stenosis shapes, namely, model I, model II, and model III, are taken into consideration to simulate the modeling with the degree of 40%, 55% and 65% blockage in order to estimate the curvature effects of stenosis on hemodynamics. The effect of pulsation, intensity of blockage, flow rate, and Womersley number is discussed in comparison to the results of momentary streamlines, axial velocity distribution, wall pressure, WSS, OSI, and RRT.

The following outcomes are derived from the present investigations.

- Rigorous numerical computations are driven to detect a grid-independent solution to give a more accurate result.
- The flow parameter, like wall pressure, is affected by the geometry of stenosis. For comparable stenosis-induced area reduction, the stenosis model III exhibits the highest wall pressure.
- Around the blockage area, the WSS of stenotic shape, namely mild contraction, exceeds that of the others.
- The disparity in the prevalence of stenotic shape on the WSS exceeds that of wall pressure across the three models.
- The intensity of WSS reaches its highest point during peak systole when the flow is maximum in the cycle.
- The immediate streamlines of flow pulsation exhibit significant changes throughout the entire cycle, marked by the vortex right after the stenotic area during the phases.
- The recirculation length in the pulsatile flow is larger at the time of deceleration.
- The recirculation zones typically happen at the same time, both near and far from the constriction, as an immediate net flow rate approaches zero.
- The recirculation length appears larger in the case of moderate contraction and right-angle expansion than in the mild contraction during the cycle.
- The disturbances of flow become more severe for greater stenosis intensity. When 65% stenosis is present, the maximum wall shear stress is 2.61 and 1.52 times greater than when 40% and 55% are present, respectively. The wall pressure also varies through the variations of the same ARs.
- The flow pattern can be greatly dominated by changes in the flow rate. A higher flow rate results in a greater wall pressure and WSS than a lower flow rate.
- Peak WSS is not significantly impacted by the Womersley number in comparison to other characteristics.

- The distributions of oscillation in terms of OSI illustrate two maxima linked to time-averaged locations of the flow's separation and reattachment.
- The reattachment site, whose location aligns with the OSI's second peak, is where RRT achieves its highest value. This point suggests an area that could develop new atherosclerotic plaque.

The influence of different stenosis models on arterial blood flow and hemodynamic characteristics shows that the changed flow patterns are crucial markers of severe atherosclerotic conditions, potentially resulting in severe cardiovascular issues such as stroke and heart failure. Although extensive research has been dedicated to symmetric, mild stenosis, upcoming studies will shift towards more intricate, realistic situations featuring multiple or asymmetrically positioned plaques. The inclusion of the impact of arterial wall flexibility will enhance the simulation model to achieve precise outcomes. In the future, advanced CFD models may be integrated with patient-based imaging data to confirm models and convert research discoveries into diagnostic instruments.

#### Nomenclature

AR area reduction

D diameter of the artery

f frequency

FSI fluid structure interaction

h constricted radius
L length of the artery

OSI oscillatory shear index

p pressure

P pulsating amplitude PSM predictive surrogate model

PWS plaque wall stress  $\bar{Q}$  mean flow rate radial coordinate

R unconstructed radius RRT relative residence time

t time T time period

TAWSS time average wall shear stress

 $egin{array}{ll} u_r & {
m radial\ velocity} \ u_z & {
m axial\ velocity} \ {
m Wo} & {
m Womersley\ number} \ {
m WSS} & {
m Wall\ shear\ stress} \ \end{array}$ 

WSSG Wall shear stress gradient

Z axial coordinate

z' dimensionless distance = Z/D

 $\rho$  density

 $\mu$  dynamic viscosity  $\tau_{wall}$  wall shear stress

## References

- [1] V. Deplano, and M. Siouffi, "Experimental and Numerical Study of Pulsatile Flows through Stenosis: Wall Shear Stress Analysis," *Journal of Biomechanics*, vol. 32, no. 10, pp. 1081-1090, 1999. [CrossRef] [Google Scholar] [Publisher Link]
- [2] Centers for Disease Control and Prevention, National Center for Chronic Disease Prevention and Health Promotion (NCCDPHP) [Online]. Available: https://www.cdc.gov/nccdphp/index.html
- [3] John M. Tarbell, "Mass Transport in Arteries and the Localization of Atherosclerosis," *Annual Review of Biomedical Engineering*, vol. 5, pp. 79-118, 2003. [CrossRef] [Google Scholar] [Publisher Link]
- [4] Saad A. Ahmed, and Don P. Giddens, "Velocity Measurements in Steady Flow through Axisymmetric Stenoses at Moderate Reynolds Numbers," *Journal of Biomechanics*, vol. 16, no. 7, pp. 505-507-509-516, 1983. [CrossRef] [Google Scholar] [Publisher Link]
- [5] Noureddine Kaid et al., "Unveiling Hemodynamic Pulsatile Flow Dynamics in Carotid Artery Stenosis: Insights from Computational Fluid Dynamics," *AIP Advances*, vol. 14, no. 6, pp. 1-13, 2024. [CrossRef] [Google Scholar] [Publisher Link]
- [6] Matadial Ojha et al., "Pulsatile Flow through Constricted Tubes: An Experimental Investigation using Photochromic Tracer Methods," *Journal of Fluid Mechanics*, vol. 203, pp. 173-197, 1989. [CrossRef] [Google Scholar] [Publisher Link]
- [7] Moloy Kumar Banerjee, Ranjan Ganguly, and Amitava Datta, "Effect of Pulsatile Flow Waveform and Womersley Number on the Flow in Stenosed Arterial Geometry," *International Scholarly Research Notices*, vol. 2012, no. 1, pp. 1-12, 2012. [CrossRef] [Google Scholar] [Publisher Link]
- [8] M.D. Deshpande, D.P. Giddens, and R.F. Mabon, "Steady Laminar Flow through Modelled Vascular Stenoses," *Journal of Biomechanicss*, vol. 9, no. 4, pp. 165-174, 1976. [CrossRef] [Google Scholar] [Publisher Link]
- [9] M. Saqib Hameed et al., "Comparison of Blood Flow Analysis in Stenosed and Stented Carotid Artery Bifurcation Models," *Cogent Engineering*, vol. 10, no. 1, pp. 1-20, 2023. [CrossRef] [Google Scholar] [Publisher Link]
- [10] M. Wootton David, and N. Ku David, "Fluid Mechanics of Vascular Systems, Diseases, and Thrombosis," *Annual Review of Biomedical Engineering*, vol. 1, pp. 299-329, 1999. [CrossRef] [Google Scholar] [Publisher Link]
- [11] Robert M. Nerem, "Hemodynamics and the Vascular Endothelium," *Journal of Biomechanical Engineering*, vol. 115, no. 4B, pp. 510-514, 1993. [CrossRef] [Google Scholar] [Publisher Link]
- [12] J.J. Chiu et al., "Effects of Disturbed Flow on Endothelial Cells," *Journal of Biomechanical Engineering*, vol. 120, no. 1, pp. 2-8, 1998. [CrossRef] [Google Scholar] [Publisher Link]
- [13] Feng Wang et al., "Linear Surrogate Modelling for Predicting Hemodynamic in Carotid Artery Stenosis During Exercise Conditions," *Chinese Journal of Physics*, vol. 94, pp. 262-273, 2025. [CrossRef] [Google Scholar] [Publisher Link]
- [14] Edith E. Alagbe et al., "Computational Simulation of Atherosclerosis Progression Associated with Blood Pressure in a 2-D Idealized Human Carotid Artery Model," *The Open Chemical Engineering Journal*, vol. 16, pp. 1-10, 2022. [CrossRef] [Google Scholar] [Publisher Link]
- [15] S.J. Sherwin, and H.M. Blackburn, "Three-Dimensional Instabilities and Transition of Steady and Pulsatile Axisymmetric Stenotic Flows," *Journal of Fluid Mechanics*, vol. 533, pp. 297-327, 2005. [CrossRef] [Google Scholar] [Publisher Link]
- [16] Byoung Jin Jeon et al., "A Numerical Study on the Effect of Trapezium Stenosis Shape on the Axisymmetric flow Field around Stenosis," *Journal of Mechanical Science and Technology*, vol. 32, pp. 2651-2658, 2018. [CrossRef] [Google Scholar] [Publisher Link]
- [17] Maria Vittoria Caruso et al., "Computational Analysis of Stenosis Geometry Effects on Right Coronary Hemodynamics," 2015 37th Annual International Conference of the IEEE Engineering in Medicine and Biology Society (EMBC), Milan, Italy, pp. 981-984, 2015. [CrossRef] [Google Scholar] [Publisher Link]
- [18] Wei Liao, T.S. Lee, and H.T. Low, "Numerical Studies of Physiological Pulsatile Flow through Constricted Tube," *International Journal of Numerical Methods for Heat & Fluid Flow*, vol. 14, no. 5, pp. 689-713, 2004. [CrossRef] [Google Scholar] [Publisher Link]
- [19] A.B.M. Toufique Hasan, and D. Kanti Das, "Numerical Simulation of Sinusoidal Fluctuated Pulsatile Laminar Flow through Stenotic Artery," *Journal of Applied Fluid Mechanics*, vol. 1, no. 2, pp. 25-35, 2012. [CrossRef] [Google Scholar] [Publisher Link]
- [20] T. Ray Mahapatra, G.C. Layek, and M.K. Maiti, "Unsteady Laminar Separated Flow through Constricted Channel," *International Journal of Nonlinear Mechanics*, vol. 37, no. 2, pp. 171-186, 2002. [CrossRef] [Google Scholar] [Publisher Link]
- [21] G.R. Zendehbudi, and M.S. Moayeri, "Comparison of Physiological and Simple Pulsatile Flows through Stenosed Arteries," *Journal of Biomechanics*, vol. 32, no. 9, pp. 959-965, 1999. [CrossRef] [Google Scholar] [Publisher Link]
- [22] Temiloluwa Amoo, Osejie Oriaifo, and Augustine Ayeni, "Computational Simulation of the Effects of Blood Flow Velocity on Atherosclerosis Progression in a Human Carotid Artery," *F1000 Research*, vol. 13, pp. 1-17, 2024. [CrossRef] [Google Scholar] [Publisher Link]
- [23] S.A. Berger, and L.D. Jou, "Flows in Stenotic Vessels," *Annual Review in Fluid Mechanics*, vol. 32, pp. 347-382, 2000. [CrossRef] [Google Scholar] [Publisher Link]
- [24] R. Mittal, S.P. Simmons, and H.S. Udaykumar, "Application of Large-Eddy Simulation to the Study of Pulsatile Flow in a Modeled Arterial Stenosis," *Journal of Biomechanical Engineering Transactions ASME*, vol. 123, no. 4, pp. 325-332, 2001. [CrossRef] [Google Scholar] [Publisher Link]

- [25] J. Satya Eswari et al., "Prediction of Stenosis Behaviour in Artery by Neural Network and Multiple Linear Regressions," *Biomechanics and Modeling in Mechanobiology*, vol. 19, pp. 1697-1711, 2020. [CrossRef] [Google Scholar] [Publisher Link]
- [26] Mahesh C. Udupa, Sunanda Saha, and Sekarapandian Natarajan, "Study of Blood Flow Patterns in a Stenosed Artery through the Combined Effect of Body Acceleration and Generalized Womersley Solution," *Scientific Reports*, vol. 15, pp. 1-18, 2025. [CrossRef] [Google Scholar] [Publisher Link]
- [27] Stefania Espa, Monica Moroni, and Maria Antonietta Boniforti, "In-Vitro Simulation of the Blood Flow in an Axisymmetric Abdominal Aortic Aneurysm," *Applied Sciences*, vol. 9, no. 21, pp. 1-16, 2019. [CrossRef] [Google Scholar] [Publisher Link]
- [28] R. Padma, R. Tamil Selvi, and R. Ponalagusamy, "Effects of Slip and Magnetic Field on the Pulsatile Flow of a Jeffrey Fluid with Magnetic Nanoparticles in a Stenosed Artery," *The European Physical Journal Plus*, vol. 134, 2019. [CrossRef] [Google Scholar] [Publisher Link]
- [29] S. Kang, H.G. Choi, and J.Y. Yoo, "Investigation of Fluid–Structure Interactions using a Velocity-Linked P2/P1 Finite Element Method and the Generalized- α Method," *International Journal for Numerical Methods in Engineering*, vol. 90, no. 12, pp. 1529-1548, 2012. [CrossRef] [Google Scholar] [Publisher Link]
- [30] D. Gallo et al. "On the Use of In Vivo Measured Flow Rates as Boundary Conditions for Image-Based Hemodynamic Models of the Human Aorta: Implications for Indicators of Abnormal Flow," *Annals of Biomedical Engineering*, vol. 40, pp. 729-741, 2012. [CrossRef] [Google Scholar] [Publisher Link]
- [31] Qinghai Huang et al., "Hemodynamic Changes by Flow Diverters in Rabbit Aneurysm Models," *Stroke*, vol. 44, no. 7, pp. 1936-1941, 2013. [CrossRef] [Google Scholar] [Publisher Link]
- [32] Panagiotis Kelidis, and Efstathios Konstantinidis, "Pulsatile Flow through a Constricted Tube: Effect of Stenosis Morphology on Hemodynamic Parameters," *Computer Methods in Biomechanics and Biomedical Engineering*, vol. 21, no. 7, pp. 479-487, 2018. [CrossRef] [Google Scholar] [Publisher Link]
- [33] Johannes V. Soulis et al., "Relative Residence Time and Oscillatory Shear Index of Non-Newtonian Flow Models in Aorta," 2011 10<sup>th</sup> International Workshop on Biomedical Engineering, Kos, Greece, pp. 1-4, 2011. [CrossRef] [Google Scholar] [Publisher Link]